Elastic wavefield tomography with probabilistic petrophysical model constraints

Odette Aragao & Paul Sava
Center for Wave Phenomena, Colorado School of Mines

ABSTRACT

Seismic exploration and characterization workflows often use elastic wavefield tomography to derive precise models of the subsurface. Unconstrained multiparameter inversion may lead to implausible models when model parameters are derived independently of one-another. We develop a method for elastic wavefield tomography that explicitly imposes petrophysical constraints to restrict updated models to a feasible region, where the model components are consistent with each other. We demonstrate that incorporating this constraint term into the objective function improves the recovered models, when compared to models obtained without constraints, or with approximate analytic contraints.

Key words: wavefield tomography, multiparameter inversion, multicomponent data, petrophysical constraints

1 INTRODUCTION

One of the greatest challenges in seismic exploration consists of estimating accurate subsurface models. Seismic tomography has recently became the standard technique for subsurface imaging at various scales, and aims to build high resolution models of physical parameters underlying wave propagation. The two main approaches to seismic tomography are traveltime tomography (Woodward, 1992; Schuster and Quintus-Bosz, 1993; Taillandier et al., 2009) and wavefield tomography (Tarantola, 1984; Mora, 1989; Biondi, 2006). Wavefield tomography shows advantages when compared to traveltime tomography because it recovers parameters with higher resolution (Tarantola, 1986; Pratt, 1999), by exploiting both kinematics and amplitudes of the observed waveforms.

Full waveform inversion (FWI) is the most promising technique among the wavefield tomography methods as it delivers highly accurate subsurface models from seismic data (Tarantola, 1984; Pratt, 1999; Sirgue et al., 2004; Virieux and Operto, 2009). FWI operates by iteratively updating an initial model, while matching the observed data with simulated data. This optimization exploits seismic wavefield modeling (forward problem) and solves the associated inverse problem by minimizing an objective function. The gradient of the objective function estimates model perturbations that progressively decrease the data residual. Here we use the adjoint state method (Plessix, 2006) to compute the data residual gradient, since this method is among the most efficient and modest in storage requirements.

Early implementations of FWI used the acoustic wave equation (Tarantola, 1984; Pratt et al., 1996; Pratt, 1999). However, acoustic FWI does not take into account elastic effects and the presence of S waves in the data. Several parameters are necessary for describing elastic models (e.g., density ρ and Lamé parameters λ and μ, or density and P and S wave velocities), and therefore elastic FWI (EFWI) to better describes the subsurface properties (Tarantola, 1988; Pratt, 1990; Plessix, 2006).

Despite the fact that FWI is the most popular seismic inversion technique nowadays, a range of challenges persist for its routine, practical application. FWI is a highly non-linear and ill-posed problem, so its convergence is subjected to local minima. Therefore, one needs to include prior information, i.e., model regularization, into the inversion process to find a plausible solution (Tikhonov and Arsenin, 1977; Tarantola, 2005; Ivanov et al., 2005). Also, the wave extrapolator can become unstable during the updating process as model updates fluctuate, thus impending inversion to further update the model.

Elastic FWI suffers from a number of practical difficulties. First, the inversion non-linearity increases when using multiple parameters. In addition, as the parameters are updated simultaneously, but independently, the model components can be physically contradictory to one-another, creating combinations of model parameters that are lithologically implausible, or even impossible. This situation may create inaccurate forward solutions and lead to poor convergence (Baumstein, 2013). Moreover, similar radiation patterns among var-

ious elastic parameters create crosstalk (Operto et al., 2013; Kamath and Tsvankin, 2016) resulting in infeasible models. Radiation pattern analysis can partially correct for crosstalk, but such analysis is ineffective in poorly illuminated areas.

In order to recover models that are consistent with each other and properly characterize the subsurface, we need to explicitly impose model constraints during the inversion (Baumstein, 2013; Peters et al., 2015; Duan and Sava, 2016; Manukyan et al., 2018). These constraints can use petrophysical information, such as that contained in well logs. Incorporating constraints into the objective function sets model space bounds, forcing the inverted models to be consistent with known physical relationships and thus represent realistic lithological units.

Duan and Sava (2016) use logarithmic barrier constraints assuming a linear relationship between the model parameters. They prove that this petrophysical constraint yields better models even if conventional regularization is not explicitly applied during the inversion. However, complex models may have a more complex, non-linear relationship between the parameters. Morever, the analytic logarithmic barrier constraint term works with user-defined parameters, and theirs selection may be arduous, especially when different geological formations are present in the same area. Thus, it is necessary to define more general and automated petrophysical constraints that provide flexibility.

We propose elastic wavefield tomography with an objective function that constrains the relationship between the Lamé parameters, λ and μ, using model probability density functions (PDFs). We demonstrate that PDFs can be incorporated as constraints into the EFWI without knowing or defining analytic relationship among the different elastic parameters. The performance of the proposed method is illustrated with a synthetic example.

2 ELASTIC WAVEFIELD TOMOGRAPHY

We consider the isotropic elastic wave equation

$$\rho\ddot{\mathbf{u}} - \lambda[\nabla(\nabla\cdot\mathbf{u})] - \mu\left[\nabla\cdot\left(\nabla\mathbf{u}+\nabla\mathbf{u}^T\right)\right] = \mathbf{f}, \quad (1)$$

where $\mathbf{u}(e,\mathbf{x},t)$ is the elastic wavefield, $\mathbf{f}(e,\mathbf{x},t)$ is the source function, $\lambda(\mathbf{x})$ and $\mu(\mathbf{x})$ are the Lamé parameters, $\rho(\mathbf{x})$ is the density and e, $\mathbf{x}$ and t are, respectively, the experiment index, the spatial location and time. Equation 1 assumes that Lamé parameters vary slowly, such that their spatial gradient can be neglected.

The waveform inversion problem is solved by minimizing an objective function $\mathcal{J}(\mathbf{u}_s,\lambda,\mu)$ consisting of three parts: a term that evaluates the misfit between the simulated and observed data $\mathcal{J}_D(\mathbf{u}_s,\lambda,\mu)$, a model regularization term $\mathcal{J}_M(\lambda,\mu)$, that enforces spatial correlation of the model parameters, and a term that enforces petrophysical model constraints $\mathcal{J}_C(\lambda,\mu)$:

$$\mathcal{J}(\mathbf{u}_s,\lambda,\mu) = \mathcal{J}_D(\mathbf{u}_s,\lambda,\mu) + \mathcal{J}_M(\lambda,\mu) + \mathcal{J}_C(\lambda,\mu). \quad (2)$$

We can define the data residual

$$\mathbf{r}_D(e,\mathbf{x},t) = \mathbf{W}_u(e,\mathbf{x},t)\mathbf{u}_s(e,\mathbf{x},t) - \mathbf{d}_{obs}(e,\mathbf{x},t), \quad (3)$$

and then the data misfit term

$$\mathcal{J}_D(\mathbf{u}_s,\lambda,\mu) = \sum_e \frac{1}{2}\left\|\mathbf{r}_D(e,\mathbf{x},t)\right\|^2, \quad (4)$$

where $\mathbf{W}_u(e,\mathbf{x},t)$ are weights that restrict the source wavefield $\mathbf{u}_s(e,\mathbf{x},t)$ to the known receiver locations, and $\mathbf{d}_{obs}(e,\mathbf{x},t)$ are the observed data.

To update the model iteratively using a gradient-based method (Tarantola, 1988), one can compute the gradient of $\mathcal{J}_D$ with respect to the model parameters λ and μ using the adjoint-state method (Plessix, 2006). This method consists of four steps:

(i) Compute the seismic wavefield $\mathbf{u}_s$ from a source function $\mathbf{f}_s$, such that $\mathbf{L}\mathbf{u}_s - \mathbf{f}_s = \mathbf{0}$, where $\mathbf{L}$ is the linear elastic wave operator from equation 1,

(ii) Compute the adjoint source $\mathbf{g}_s = \partial\mathcal{J}/\partial\mathbf{u}_s$, which exploits the difference between observed and simulated data (equation 3),

(iii) Compute the adjoint wavefield $\mathbf{a}_s = \mathbf{L}^T\mathbf{g}_s$, which exploits the adjoint elastic wave operator $\mathbf{L}^T$,

(iv) Compute the gradient of $\mathcal{J}_D$ with respect to the parameters λ and μ by

$$\begin{bmatrix}\frac{\partial\mathcal{J}_D}{\partial\lambda}\\ \frac{\partial\mathcal{J}_D}{\partial\mu}\end{bmatrix} = \sum_e \begin{bmatrix}-\nabla(\nabla\cdot\mathbf{u})\star\mathbf{a}_s\\ -\nabla\left(\nabla\mathbf{u}+\nabla\mathbf{u}^T\right)\star\mathbf{a}_s\end{bmatrix}, \quad (5)$$

where the symbol $\star$ represents zero-lag time crosscorrelation.

Incorporating a model regularization term to the objective function reduces the inversion ill-posedness, and helps accelerate convergence towards the global minimum (Asnaashari et al., 2013). Prior information can be estimated from non-seismic data, e.g. well logs, or by incorporating knowledge about the model geometry, e.g., smoothness or consistency with a migrated image. Considering the model residuals:

$$\mathbf{r}_\lambda(\mathbf{x}) = \mathbf{W}_\lambda(\mathbf{x})(\lambda(\mathbf{x}) - \bar{\lambda}(\mathbf{x})), \quad (6)$$

$$\mathbf{r}_\mu(\mathbf{x}) = \mathbf{W}_\mu(\mathbf{x})(\mu(\mathbf{x}) - \bar{\mu}(\mathbf{x})), \quad (7)$$

the term $\mathcal{J}_M(\lambda,\mu)$ is expressed as

$$\mathcal{J}_M(\lambda,\mu) = \frac{1}{2}\left\|\mathbf{r}_\lambda(\mathbf{x})\right\|^2 + \frac{1}{2}\left\|\mathbf{r}_\mu(\mathbf{x})\right\|^2, \quad (8)$$

where $\bar{\lambda}(\mathbf{x})$ and $\bar{\mu}(\mathbf{x})$ are prior (reference) models. The weighting operators $\mathbf{W}_\lambda(\mathbf{x})$ and $\mathbf{W}_\mu(\mathbf{x})$ are related to the model covariance matrices such that $\mathbf{W}_\lambda(\mathbf{x}) = \mathbf{C}_\lambda^{-\frac{1}{2}}(\mathbf{x})$ and $\mathbf{W}_\mu(\mathbf{x}) = \mathbf{C}_\mu^{-\frac{1}{2}}(\mathbf{x})$.

The gradient of $\mathcal{J}_M(\lambda,\mu)$ with respect to the model parameters λ and μ is

$$\begin{bmatrix} \frac{\partial \mathcal{J}_M}{\partial \lambda} \\ \frac{\partial \mathcal{J}_M}{\partial \mu} \end{bmatrix} = \begin{bmatrix} \mathbf{W}_\lambda^T \mathbf{W}_\lambda (\lambda - \bar{\lambda}) \\ \mathbf{W}_\mu^T \mathbf{W}_\mu (\mu - \bar{\mu}) \end{bmatrix} \tag{9}$$

It is aparent from equations 5 and 9 that the model components for multiparameter inversion, λ and μ, are updated independently and thus can become physically inconsistent with each other, producing inaccurate images and consequently leading to inaccurate geologic interpretation. Explicity incorporating petrophysical constraints improves the quality of the inversion by restricting the updated models to a feasible region, resulting in more accurate subsurface characterization.

Duan and Sava (2016) propose the following logarithmic penalty function $\mathcal{J}_{C_L}$ to constrain the inversion to a feasible region by using physical relationships between the updated model parameters:

$$\mathcal{J}_{C_L}(\lambda, \mu) = -\eta \sum_{\mathbf{x}} \left[\log(h_u) + \log(h_l) \right]. \tag{10}$$

The scalar parameter η determines the strength of the constraint term in the objective function, and h_u and h_l are linear functions that define, respectively, upper and lower boundaries of the feasible region:

$$h_u = -\lambda + c_u \beta + b_u = 0, \tag{11}$$

$$h_l = \lambda - c_l \beta - b_l = 0. \tag{12}$$

The coefficients c_u and c_l are the slopes of the boundary lines and b_u and b_l are their intercepts. The distance of a given model parameter in the parameter space $\{\lambda, \mu\}$ to the boundary lines h_u and h_l determines the value of $\mathcal{J}_{C_L}$, such that this term dominates the objective function when models are close to either one of the barriers. This constraint forces the inverted models to move away from that line, thus acting like a barrier that restricts the models to the feasible region.

The gradients of $\mathcal{J}_{C_L}$ with respect to the model parameters λ and μ are

$$\begin{bmatrix} \frac{\partial \mathcal{J}_{C_L}}{\partial \lambda} \\ \frac{\partial \mathcal{J}_{C_L}}{\partial \mu} \end{bmatrix} = \begin{bmatrix} \frac{-\eta}{\lambda - c_u \mu - b_u} - \frac{\eta}{\lambda - c_l \mu - b_l} \\ \frac{\eta c_u}{\lambda - c_u \mu - b_u} + \frac{\eta c_l}{\lambda - c_l \mu - b_l} \end{bmatrix}. \tag{13}$$

The term $\mathcal{J}_{C_L}$ assumes that the relationship between the model parameters λ and μ is linear, which may not be true for complex models. Alternatively, if we have access to petrophysical information obtained, for example, from well logs, we can impose a more general kind of petrophysical constraint. One can construct a model probability density function (PDF) using a normalized histogram of the reference well log parameters to characterize the dependence between the elastic model parameters.

Consider, for example, the crossplot in Figure 1(a) illustrating a possible petrophysical relationship between the Lamé parameters, λ and μ. The linear barrier constraint $\mathcal{J}_{C_L}$ would not be appropriate for this example, as λ and μ do not share a linear relationship. Instead, we can create a model PDF (Figure 1(b)) based on the available values of λ and μ. For any given model with components (λ_x, μ_x), represented by the red dot in Figure 1(b), we would like to evaluate a model space distance to the entire distribution (Figure 2). If this point is close to regions of high probabilities, we would like the value of the petrophysical constraint $\mathcal{J}_{C_P}$ to be small. Otherwise, the value of $\mathcal{J}_{C_P}$ must be large and increasing when model parameters separate more from the center of the distribution. To accomplish this, we construct a weighted sum of the distance between (λ_x, μ_x) to all the points of the PDF. The weight is proportional to the value of the PDF in a specific model cell and inverse proportional to the distance from the analyzed model to that cell.

The distance, in the model parameter space, from (λ_x, μ_x) to a cell of the PDF with indices (i, j) is

$$d_x(i,j) = \sqrt{[\lambda(i) - \lambda_x]^2 + [\mu(j) - \mu_x]^2}, \tag{14}$$

for $i = 1, \cdots, N_\lambda$ and $j = 1, \cdots, N_\mu$. Then, the weight from a specific model (λ_x, μ_x) to the cell at coordinates (i, j) with the probability $P(i, j)$ is

$$w_x(i,j) = \frac{P(i,j)}{d_x(i,j)}. \tag{15}$$

Figure 1(c) shows the distribution of w_x for the model PDF in Figure 1(b), where the red dot represents the model with components (λ_x, μ_x). The weighted distance from the point (λ_x, μ_x) to the entire distribution is

$$D_{\mathbf{x}} = \sum_{i,j} \left[\frac{P(i,j)}{d_x(i,j)} \right]. \tag{16}$$

Therefore, each point in the updated model space is connected to all cells of the model PDF, i.e., we have constructed the distance from this model to the distribution. Since $D_{\mathbf{x}}$ is small for points that are far from regions of high probabilities, and we want the value of the petrophysical constraint $\mathcal{J}_{C_P}$ to be large for this case, we can define the constraint term $\mathcal{J}_{C_P}$ as

$$\mathcal{J}_{C_P}(\lambda, \mu) = \eta \sum_{\mathbf{x}} \frac{1}{D_{\mathbf{x}}}. \tag{17}$$

This definition imposes the condition that all points representing inverted models are as close as possible to the original petrophysical distribution without being drawn especially to any value of the model, but rather close to the entire distribution. Figure 1(d) shows the distribution of the constraint term calculated using equation 17 and the PDF presented in Figure 1(b).

The gradient of $\mathcal{J}_{C_P}$ with respect to the model parameters λ and μ is

$$\begin{bmatrix} \frac{\partial \mathcal{J}_{C_P}}{\partial \lambda} \\ \frac{\partial \mathcal{J}_{C_P}}{\partial \mu} \end{bmatrix} = -\eta \begin{bmatrix} \left(\sum_{i,j} \frac{P(i,j)[\lambda(i) - \lambda_x]}{[d_x(i,j)]^3} \right) \sum_{i,j} \frac{1}{D_{\mathbf{x}}^{-2}} \\ \left(\sum_{i,j} \frac{P(i,j)[\mu(j) - \mu_x]}{[d_x(i,j)]^3} \right) \sum_{i,j} \frac{1}{D_{\mathbf{x}}^{-2}} \end{bmatrix}. \tag{18}$$

The distance to high probabilities in the model parameter space defines the value of $\mathcal{J}_{C_P}$, such that the gradient of this term dominates in the total gradient of the objective function $\mathcal{J}$ if the updated models are far from high probabilities. Otherwise, this term smoothly it forces the models away from regions of low probability.

3 EXAMPLES

We illustrate our EFWI method with one synthetic example and compare inversion using only the data misfit term $\mathcal{J}_D$ with inversion using the data misfit with the linear barrier constraint $\mathcal{J}_D + \mathcal{J}_{C_L}$, and inversion using the data misfit with the probabilistic constraint $\mathcal{J}_D + \mathcal{J}_{C_P}$.

The synthetic models contain one negative and one positive Gaussian anomalies centered at $(1.25, 0.75)$ and $(1.25, 1.75)$ km, respectively. There are 20 vertical displacement sources in a well at $x = 0.1$ km and a line of geophones at $x = 2.4$ km (Figure 3). We choose this simple example to show how the inversion using data misfit with the linear barrier constraint fails when there are two clusters, which represent two lithological sets with different linear relationships between the parameters λ and μ.

Figures 4(a) and 5(a) show the true λ and μ models, respectively. The PDF of the true λ and μ models is shown in Figure 6(a), with feasible region used in the probabilistic inversion plotted in green. The model with coordinates $(10.388, 5.19)$ GPa in the model parameter space corresponds to the background. For simplicity, we define the PDF as a Gaussian distribution covering the true model. This is not necessary for more complex examples, where the relationship among the parameters is non-linear and derived from actual well logs. We use as initial model the constant background from the true model.

Figures 4(b), 4(c) and 4(d) show the recovered λ models using the objective functions $\mathcal{J}_D$, $\mathcal{J}_D + \mathcal{J}_{C_L}$ and $\mathcal{J}_D + \mathcal{J}_{C_P}$, respectively, after 10 iterations. Notice that we recover better the true λ model (Figure 4(a)) when we include the probabilistic constraint term $\mathcal{J}_{C_P}$ in the objective function (Figure 4(d)). Figures 5(b), 5(c) and 5(d) show the the recovered μ models using the objective function as $\mathcal{J}_D$, $\mathcal{J}_D + \mathcal{J}_{C_L}$ and $\mathcal{J}_D + \mathcal{J}_{C_P}$, respectively. Note that both anomalies have amplitude and shape closer to the true model (Figure 5(a)) when we include the probabilistic constraint term $\mathcal{J}_{C_P}$ in the objective function (Figure 5(d)).

Figures 6(b), 6(c) and 6(d) show the $\lambda - \mu$ PDF of the inverted models, using the objective function as $\mathcal{J}_D$, $\mathcal{J}_D + \mathcal{J}_{C_L}$ and $\mathcal{J}_D + \mathcal{J}_{C_P}$, respectively. The green lines in Figures 6(c) and 6(d) correspond to the linear boundaries used to define the logarithmic penalty function of $\mathcal{J}_{C_L}$ and the feasible region used to define the probabilistic constraint $\mathcal{J}_{C_P}$, respectively. Without imposing petrophysical constraints (Figure 6(b)), the λ and μ values deviate from the true model (Figure 6(a)). The linear barriers restrict the relationship between λ and μ to the region delimited by the barriers (Figure 6(c)). As $\mathcal{J}_{C_L}$ uses a logarithmic penalty function, it forces all recovered models towards the middle area between the linear boundaries. The point $(10.388, 5.19)$ GPa, which represents the background model, is not in the middle between the two boundaries and, consequently, the inversion using $\mathcal{J}_{C_L}$ changes the background (Figures 4(c) and 5(c)). Imposing the probabilistic constraint confines the model to the feasible region and thus recovers better λ and μ models (Figure 6(d)).

Vertical profiles from inverted λ and μ models at $x = 1.25$ km are shown in Figure 7, where the black lines indicate the true models and the colored lines are the recovered models for the three objective functions. Using the objective function $\mathcal{J}_D$, we obtain a reliable model update for μ (Figure 7(d)), but an incorrect model update for λ (Figure 7(a)). Using the objective function $\mathcal{J}_D + \mathcal{J}_{C_L}$, we distort the background values and do not recover the anomalies (Figures 7(b) and 7(e)). Using the petrophysical constraint, we obtain models that better represent the true models (Figures 7(c) and 7(f)), without negatively affecting the background model.

Another vertical profile located at $x = 1.0$ km is shown in Figure 8. This indicates even better that more accurate λ and μ models are recovered using the probabilistic constraints (Figures 8(c) and 8(f)). In this example, using the objective function $\mathcal{J}_D$ leads to an incorrect model update for μ (Figure 8(d)).

.

4 CONCLUSIONS

We demonstrate that imposing petrophysical constraints in elastic wavefield tomography improves the quality of the recovered models, by restricting them to a feasible region, and therefore guiding the inversion towards geologically-plausible solutions. We develop a strategy for incorporating petrophysical information into the elastic full-waveform inversion, through model probability density functions in the EFWI objective function. A synthetic example with multiple anomalies shows that the models recovered with the proposed method are closer to the true models, while maintaining robust and realistic petrophysical relationships between the model parameters.

5 ACKNOWLEDGMENTS

We acknowledge CAPES (Brazilian Federal Agency for Support and Evaluation of Graduate Education) for financial support. We thank the sponsors of the Center for Wave Phenomena (CWP), whose support made this research possible. We acknowledge Daniel Rocha, Ivan Lin and Tuğrul Konuk for helpful discussions. The synthetic example in this paper uses the Madagascar open-source software package (Fomel et al., 2013) freely available from http://www.ahay.org.

REFERENCES

Asnaashari, A., R. Brossier, S. Garambois, F. Audebert, P. Thore, and J. Virieux, 2013, Regularized seismic full wave-

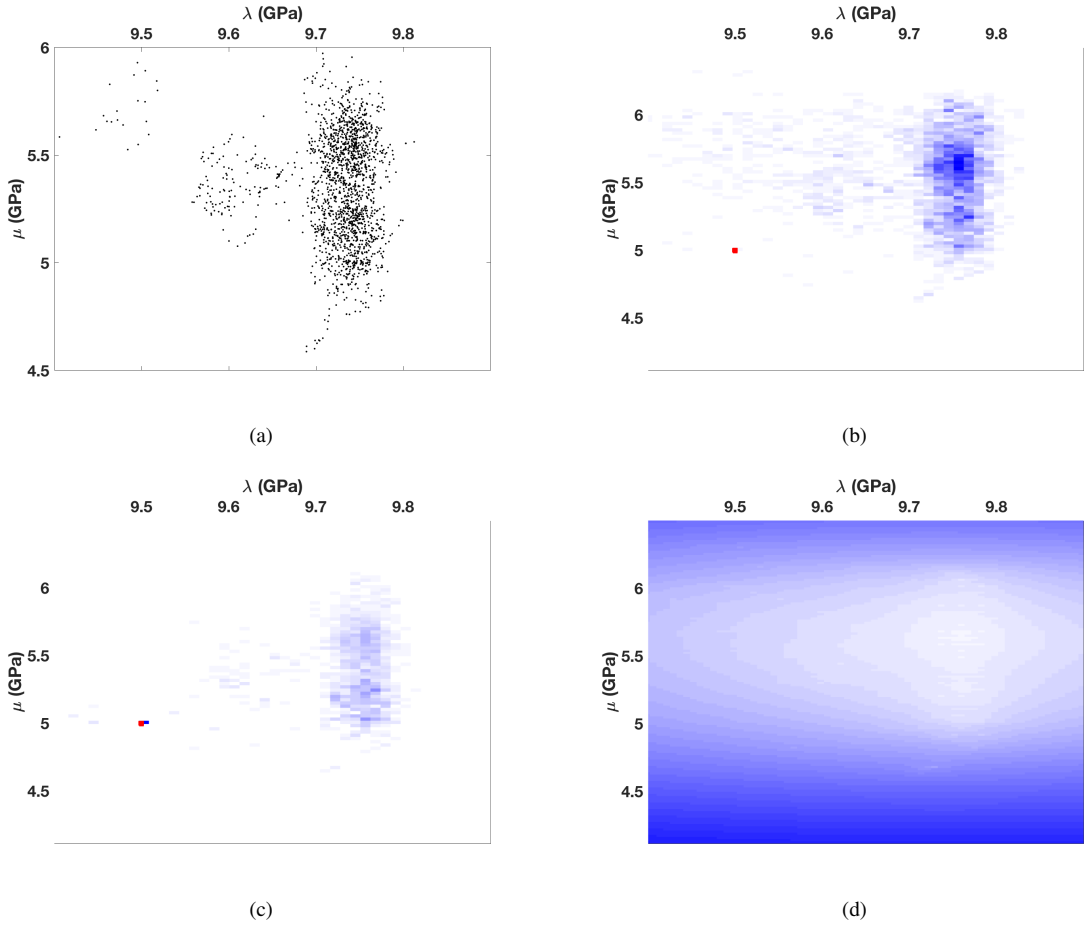

Figure 1. (a) Example of a λ and μ crossplot. (b) Model PDF associated to the crossplot in (a), that characterizes the dependency between λ and μ. The red dot represent a specific model with components (λ_x, μ_x). (c) The distribution of w_x for the model shown in (b). (d) The distribution of the constraint term calculated with Equation 17 associated to the PDF in (b). Note that high probability models are associated with low values for the constraint.

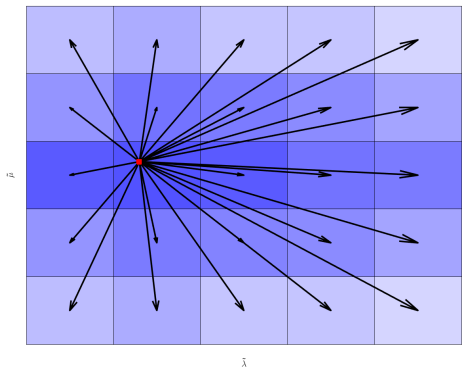

Figure 2. Sketch indicating how each point in the updated model space (red dot) communicates with all cells of the model PDF. Each cell of the model PDF contributes proportionally with its probability value and inverse proportionally to the distance to the analyzed model.

form inversion with prior model information: Geophysics, **78**, R25–R36.

Baumstein, A., 2013, POCS-based geophysical constraints in multiparameter full wavefield inversion: Presented at the 75th European Association of Geoscientists and Engineers Conference and Exhibition.

Biondi, B., 2006, 3-d seismic imaging: Society of Exploration Geophysics.

Duan, Y., and P. Sava, 2016, Elastic wavefield tomography with physical model constraints: Geophysics, **81**, no. 6, R447–R456.

Fomel, S., P. Sava, I. Vlad, Y. Liu, and V. Bashkardin, 2013, Madagascar: open-source software project for multidimensional data analysis and reproducible computational experiments: Journal of Open Research Software, 8th ed., DOI: http://dx.doi.org/10.5334/jors.ag.

Ivanov, J., R. Miller, J. Xia, D. Steeples, and C. B. Park, 2005, The inverse problem of refraction travel times. Part I: Types of geophysical nonuniquiness through minimization: Pure and Applied Geophysics, **162**, no. 3, 447–459.

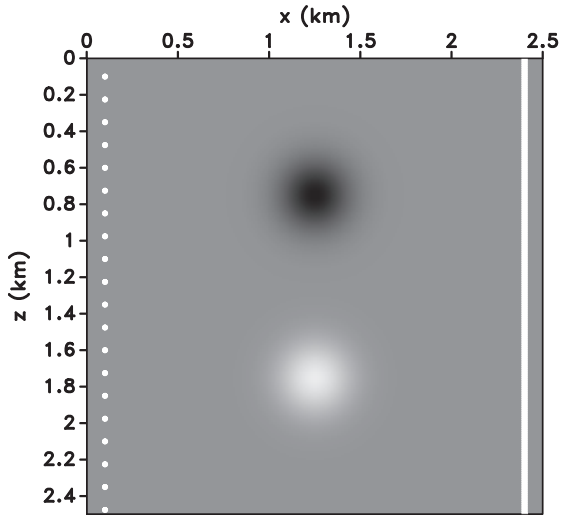

Figure 3. Acquistion geometry for the synthetic example. The dots represent source locations at $x = 0.1\,\text{km}$, and the vertical line corresponds to the receivers at $x = 1.9\,\text{km}$. The negative and positive Gaussian anomalies for the λ and μ models are centered at $(1.25, 0.75)$ and $(1.25, 1.75)$ km, respectively.

Kamath, N., and I. Tsvankin, 2016, Elastic full-waveform inversion for VTI media: methodology and sensitivity analysis: Geophysics, **81**, no. 2, C53–C68.

Manukyan, E., H. Maurer, and A. Nuber, 2018, Improvements to elastic full-waveform inversion using cross-gradient constraints: Geophysics, **83**, no. 2, R105–R115.

Mora, P., 1989, Inversion = migration + tomography: Geophysics, **54**, 1575–1586.

Operto, S., Y. Gholami, V. Prieux, A. Ribodetti, R. Brossier, L. Metivier, and J. Virieux, 2013, A guided tour of multiparameter full-waveform inversion with multicomponent data: from theory to practice: The Leading Edge, **32**, no. 9, 1040–1054.

Peters, B., Z. Fang, B. R. Smithyman, and F. J. Herrmann, 2015, Regularizing waveform inversion by projections onto convex sets - application to the 2D Chevron 2014 synthetic blind-test dataset: University of British Columbia - Seismic Laboratory for Imaging and Modeling - Research Report.

Plessix, R. E., 2006, A review of the adjoint-state method for computing the gradient of a functional with geophysical applications: Geophysical Journal International, **167**, no. 2, 495–503.

Pratt, R. G., 1990, Inverse theory applied to multi-source cross-hole tomography: Geophysical Prospecting, **38**, 311–329.

———, 1999, Seismic waveform inversion in the frequency domain. Part 1: Theory and verification in a physical scale model: Geophysics, **64**, 888–901.

Pratt, R. G., Z. M. Williamson, and M. Warner, 1996, Two-dimensional velocity model from wide-angle seismic data by wavefield inversion: Geophysical Journal International, **124**, 323–340.

Schuster, G. T., and A. Quintus-Bosz, 1993, Wavepath eikonal traveltime inversion: Theory: Geophysics, **58**, 1314–1323.

Sirgue, L., , and R. Pratt, 2004, Efficient waveform inversion and imaging: a strategy for selecting temporal frequencies: Geophysics, **69**, 231–248.

Taillandier, C. M., M. Noble, H. Chauris, and H. Calandra, 2009, First-arrival traveltime tomography based on the adjoint-state method: Geophysics, **74**, WCB1–WCB10.

Tarantola, A., 1984, Inversion of seismic reflection data in the acoustic approximation: Geophysics, **49**, 1259–1266.

———, 1986, A strategy for nonlinear elastic inversion of seismic reflection data: Geophysics, **51**, 1893–1903.

———, 1988, Theoretical background for the inversion of seismic waveforms including elasticity and attenuation: Pure and Applied Geophysics, **128**, 365–399.

———, 2005, Inverse Problem Theory and Methods for Model Parameter Estimation: Society for Industrial and Applied Mathematics.

Tikhonov, A., and V. Arsenin, 1977, Solution of ill-posed problems: Winston and Sons.

Virieux, J., and S. Operto, 2009, An overview of full-waveform inversion in exploration geophysics: Geophysics, **74**, no. 6, WCC1–WCC26.

Woodward, M. J., 1992, Wave-equation tomography: Geophysics, **57**, 15–26.

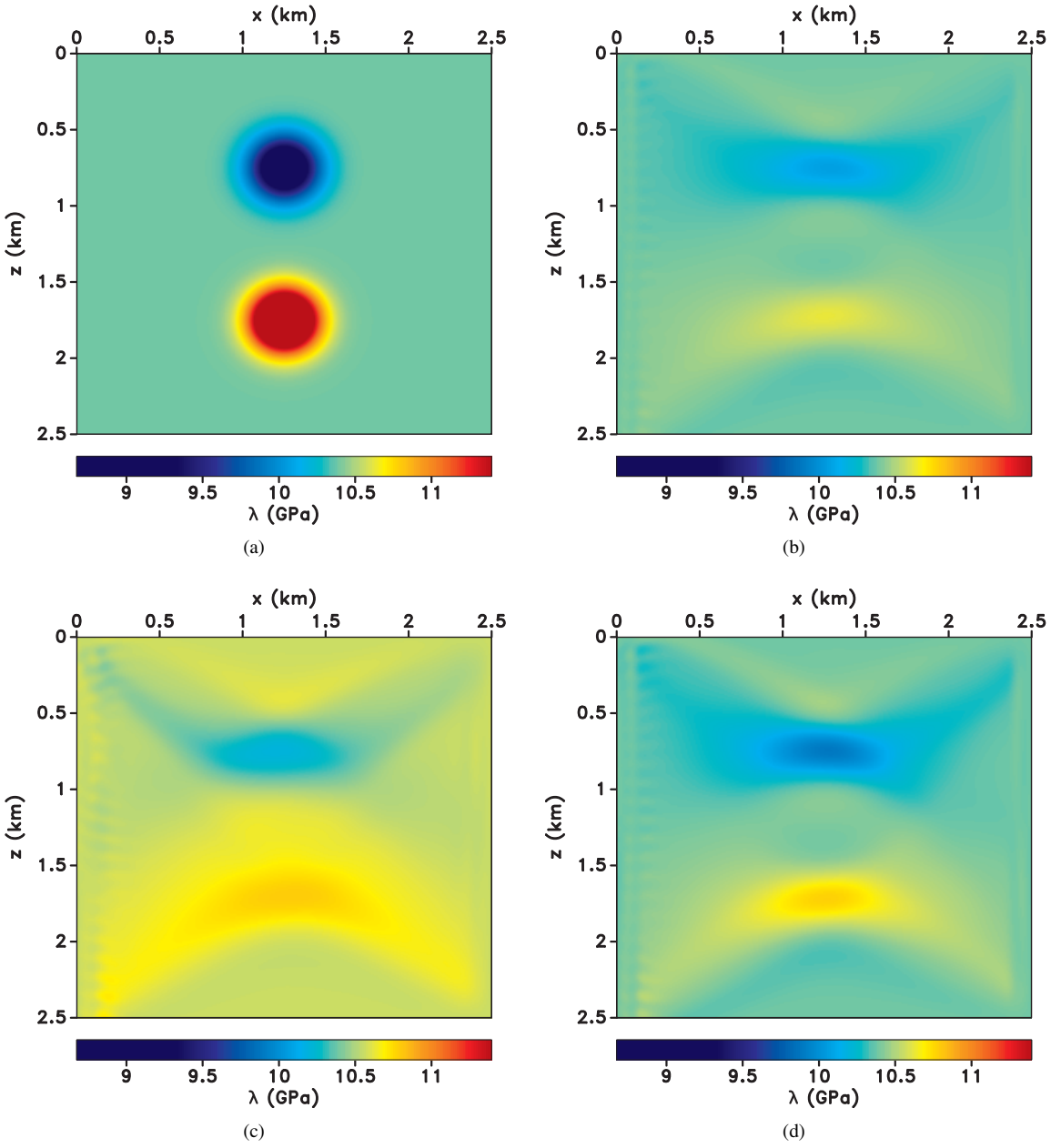

Figure 4. (a) True λ model and updated λ models using the objective function (b) $\mathcal{J}_D$, (c) $\mathcal{J}_D + \mathcal{J}_{C_L}$ and (d) $\mathcal{J}_D + \mathcal{J}_{C_P}$. Notice that the Gaussian anomalies in (a) are better recovered in (d) than in (b) and (c).

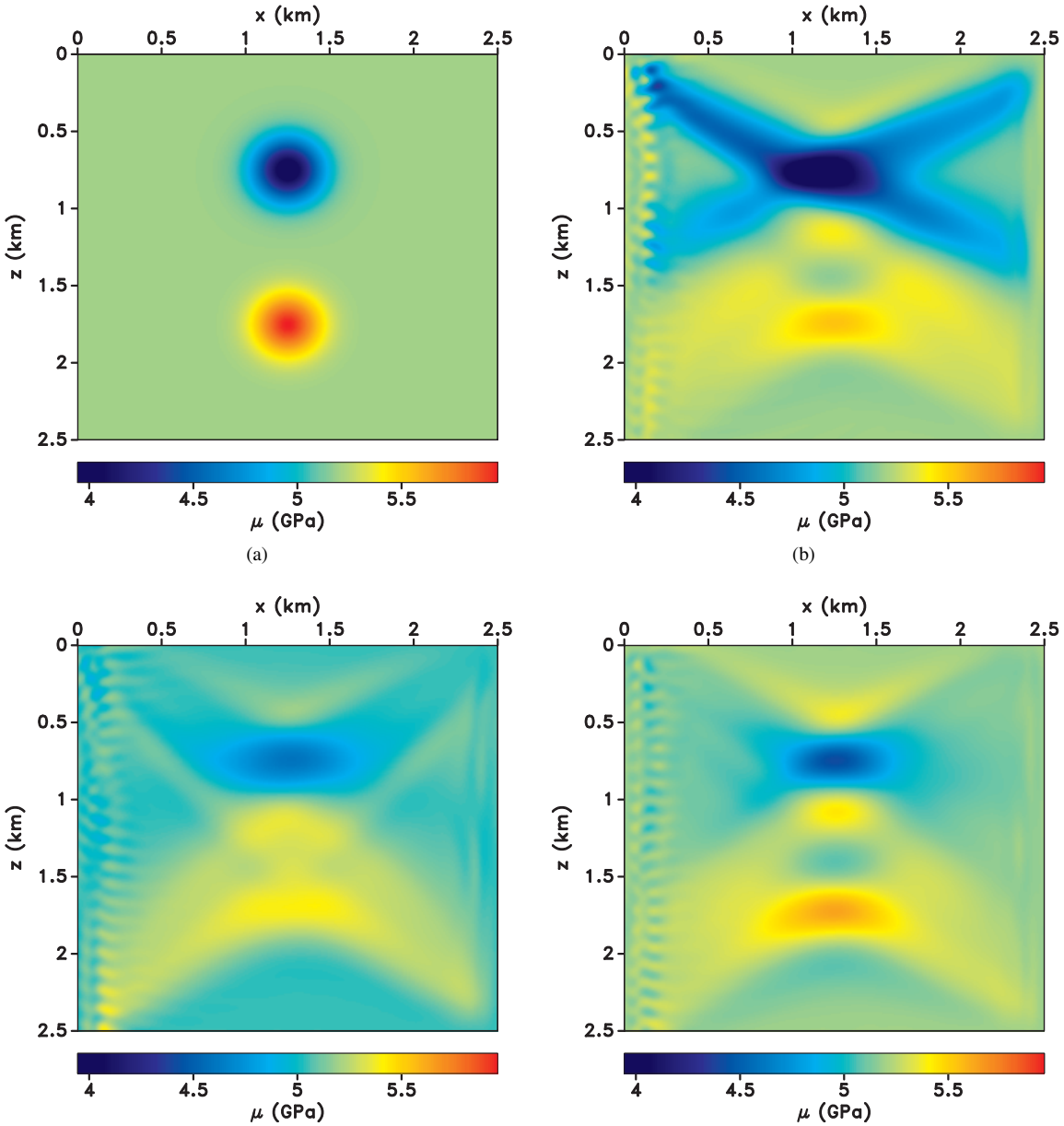

Figure 5. (a) True μ model and updated μ models using the objective function (b) $\mathcal{J}_D$, (c) $\mathcal{J}_D + \mathcal{J}_{C_L}$ and (d) $\mathcal{J}_D + \mathcal{J}_{C_P}$. Note that the μ model in (d) is better recovered than the models in (b) or (c).

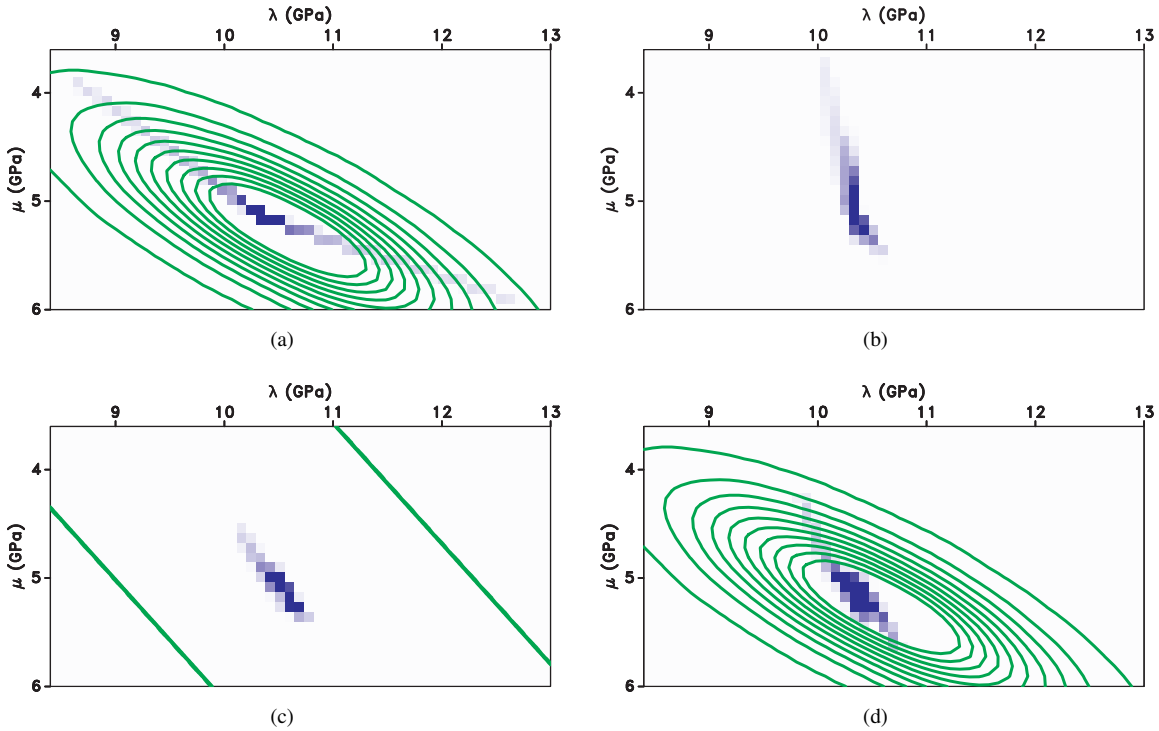

Figure 6. PDF of λ and μ for (a) the true model and for the updated models using the objective function (b) $\mathcal{J}_D$, (c) $\mathcal{J}_D + \mathcal{J}_{C_L}$ and (d) $\mathcal{J}_D + \mathcal{J}_{C_P}$. The green contours in (a) and (d) represent the feasible area for the probabilistic constraint. The green lines in (c) define the upper and lower boundaries used in the logarithmic penalty function $\mathcal{J}_{C_L}$

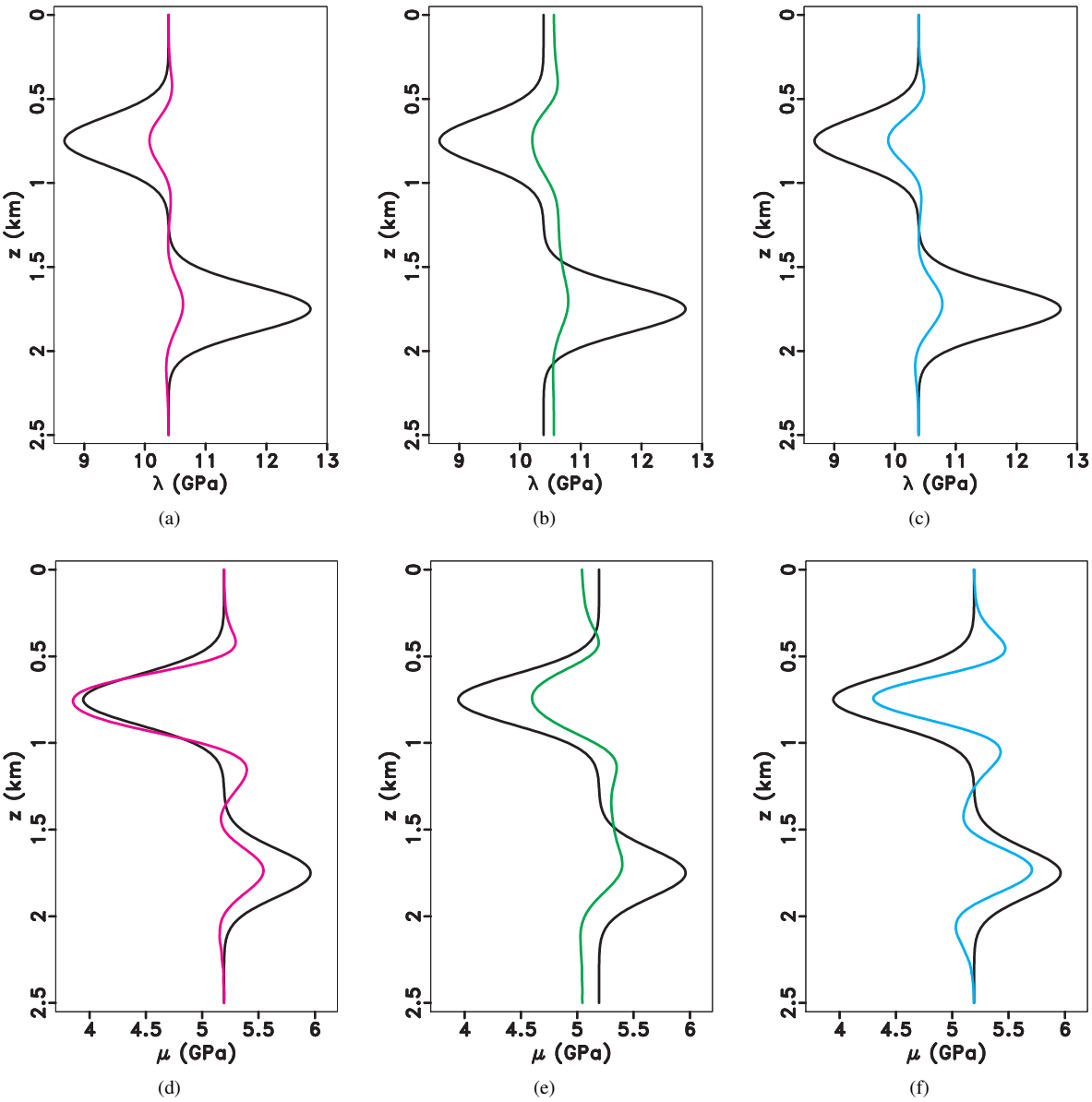

Figure 7. Comparison between true models and recovered models from a vertical profile at $x = 1.25$ km. Row one: black lines are the true λ model and colored lines are the updated models using the objective function (a) $\mathcal{J}_D$ (red line), (b) $\mathcal{J}_D + \mathcal{J}_{C_L}$ (green line) and (c) $\mathcal{J}_D + \mathcal{J}_{C_P}$ (blue line). Row two: black lines are the true μ model and colored lines are the updated models using the objective function as (d) $\mathcal{J}_D$ (red line), (e) $\mathcal{J}_D + \mathcal{J}_{C_L}$ (green line) and (f) $\mathcal{J}_D + \mathcal{J}_{C_P}$ (blue line).

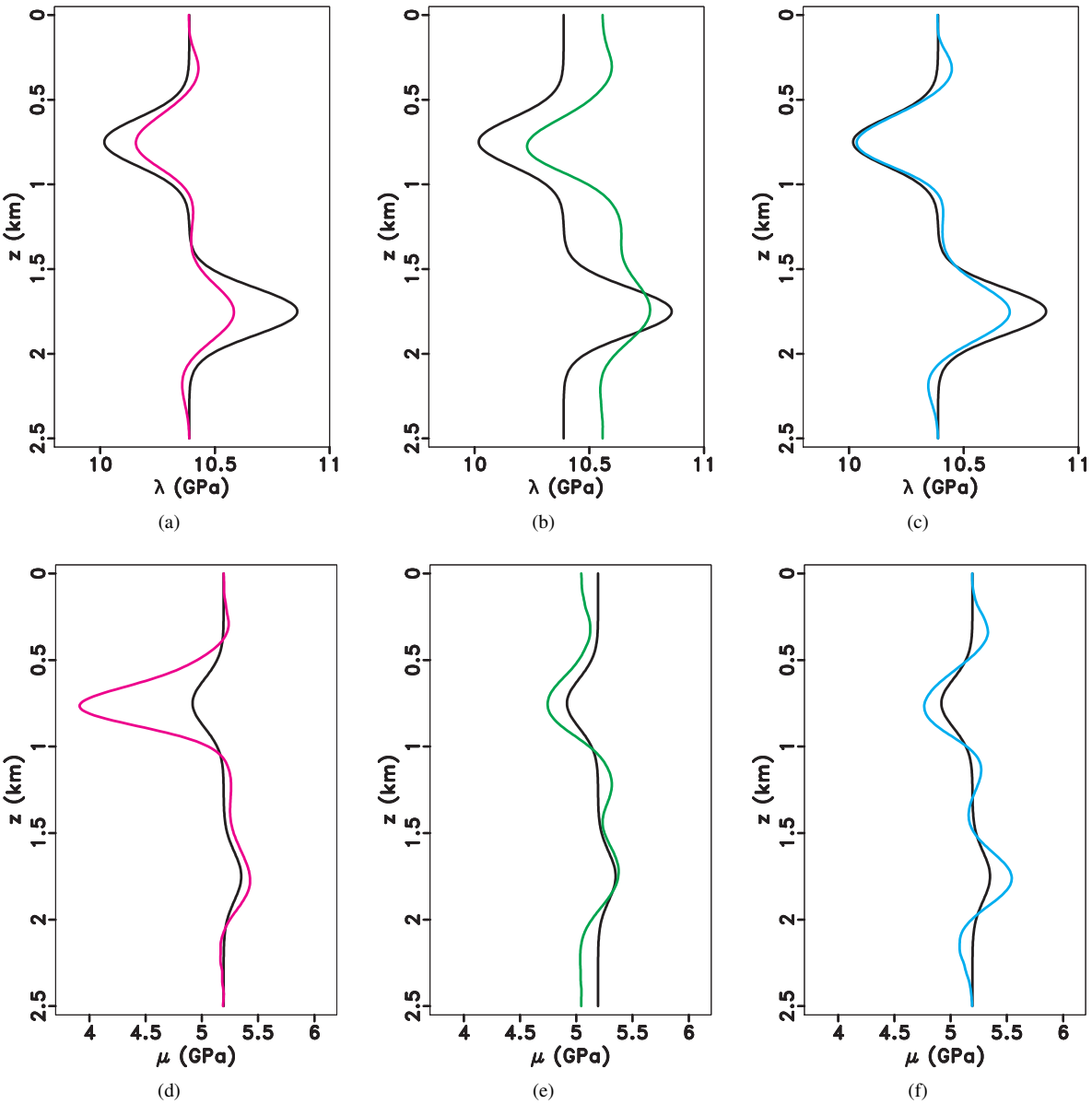

Figure 8. Comparison between true models and recovered models from a vertical profile at $x = 1.0$ km. Row one: black lines are the true λ model and colored lines are the updated models using the objective function (a) $\mathcal{J}_D$ (red line), (b) $\mathcal{J}_D + \mathcal{J}_{C_L}$ (green line) and (c) $\mathcal{J}_D + \mathcal{J}_{C_P}$ (blue line). Row two: black lines are the true μ model and colored lines are the updated models using the objective function as (d) $\mathcal{J}_D$ (red line), (e) $\mathcal{J}_D + \mathcal{J}_{C_L}$ (green line) and (f) $\mathcal{J}_D + \mathcal{J}_{C_P}$ (blue line).